

Research Article

Open Access



Evidence of shear stress component in Lüders front based on an *in-situ* synchrotron high-energy X-ray diffraction experiment

Minghe Zhang¹, Junrou Jia¹, Zhennan Jia¹, Yunli Feng¹, Ziyu Ma², Yan-Dong Wang³, Runguang Li^{2,3}

¹College of Metallurgy and Energy, North China University of Science and Technology, Tangshan 063210, Hebei, China.

²Institute for Frontier Materials, Deakin University, Geelong, VIC 3216, Australia.

³Beijing Advanced Innovation Center for Materials Genome Engineering, State Key Laboratory for Advanced Metals and Materials, University of Science and Technology Beijing, Beijing 100083, China.

Correspondence to: Dr. Runguang Li, Institute for Frontier Materials, Deakin University, 75 Pigdons Road, Waurin Ponds, VIC 3216, Australia; Beijing Advanced Innovation Center for Materials Genome Engineering, State Key Laboratory for Advanced Metals and Materials, University of Science and Technology Beijing, 30 Xueyuan Road, Haidian District, Beijing 100083, China.
E-mail: runguang.li@deakin.edu.au

How to cite this article: Zhang, M.; Jia, J.; Jia, Z.; Feng, Y.; Ma, Z.; Wang, Y. D.; Li, R. Evidence of shear stress component in Lüders front based on an *in-situ* synchrotron high-energy X-ray diffraction experiment. *Microstructures* 2025, 5, 2025099. <https://dx.doi.org/10.20517/microstructures.2025.38>

Received: 20 Mar 2025 **First Decision:** 8 Jul 2025 **Revised:** 12 Jul 2025 **Accepted:** 25 Jul 2025 **Published:** 14 Nov 2025

Academic Editor: Danmin Liu **Copy Editor:** Fangling Lan **Production Editor:** Fangling Lan

Abstract

The formation and propagation of Lüders bands are important phenomena in the plastic deformation of some critical structural materials. The propagating Lüders front, which is structurally unstable, plays a key role in this process. Yet, the microstructural and stress states of the Lüders front are challenging to characterize and remain insufficiently understood. The present study utilized *in-situ* synchrotron-based high-energy X-ray diffraction on a fine-grained medium-Mn transformation-induced plasticity steel exhibiting typical Lüders banding behavior. Detailed analysis of evolving diffraction patterns was performed regarding peak intensity, full width at half maximum, and measured lattice strain. An abnormal measured lattice strain asymmetry was observed from the Debye rings that were collected when the Lüders front overlapped with the irradiated volume. This allows for a discussion of the local microstructural and stress states of the Lüders front, evidencing the possibility of a local shear stress component with a tilted principal stress axis. The work offers new insights into the micro-mechanisms of Lüders banding. It provides a practical and efficient analytical method for studying the dynamics of localized deformations, particularly when deformation is inhomogeneous within the characterized volume or inconsistent with macroscopic deformation.

Keywords: Synchrotron X-ray diffraction, medium-Mn steel, Lüders bands, shear stress



© The Author(s) 2025. **Open Access** This article is licensed under a Creative Commons Attribution 4.0 International License (<https://creativecommons.org/licenses/by/4.0/>), which permits unrestricted use, sharing, adaptation, distribution and reproduction in any medium or format, for any purpose, even commercially, as long as you give appropriate credit to the original author(s) and the source, provide a link to the Creative Commons license, and indicate if changes were made.



INTRODUCTION

Medium-Mn steels (typically containing 3–12 wt.% Mn) have attracted considerable attention from both academic researchers and the automotive industry owing to their outstanding combination of mechanical properties and cost-effectiveness in production^[1–6]. Exceptional performance has been achieved in medium-Mn steels through meticulous composition design and optimized manufacturing processes such as hot and/or cold rolling, intercritical annealing, and low-temperature tempering, realizing impressive tensile strengths of up to 1,500 MPa, coupled with remarkable ductility exceeding 40%^[7–10]. These attributes make the steel highly appealing for applications requiring strength and formability, particularly in automotive structures.

Despite the advantages mentioned above, the appearance of Lüders bands in medium-Mn steels during the deformation stage presents a notable challenge, especially after undergoing cold rolling and critical annealing^[11–14]. Lüders banding manifests as localized deformation bands that propagate across the material under stress, leading to undesirable visual defects such as stretch marks during the sheet-forming process^[15–18]. These surface irregularities compromise the aesthetic quality of formed components and trigger localized strain concentrations that adversely affect the uniformity and overall mechanical performance of the material. Moreover, the localized and propagative nature of the Lüders bands undermines the mechanical integrity by introducing inconsistencies in the stress distribution during deformation^[19–24]. These issues highlight the pressing need to investigate the underlying mechanisms driving the formation and propagation of Lüders bands. Understanding these mechanisms is crucial for developing effective strategies to suppress Lüders banding in medium-Mn steels and other alloys, enhancing their suitability in high-performance forming processes.

The study of Lüders band formation and propagation holds substantial importance in materials science and engineering due to its impact on material behavior during plastic deformation^[25–27]. Luo *et al.* investigated the influence of the initial microstructure and critical annealing temperature on the tensile properties and Lüders strain of medium-Mn steels, finding that the proportion and size of austenite grains, as well as the amount of carbide formed during critical annealing, are key microstructure factors that govern Lüders strain^[28]. Zhang *et al.* utilized *in-situ* high-energy X-ray diffraction (HE-XRD) to reveal the two-dimensional distribution of the austenite around Lüders bands during the transformation-induced plasticity (TRIP) deformation of medium-Mn steels, demonstrating that the propagation of Lüders bands promoted the austenite-martensite transformation, accompanied by complex stress change^[29]. Recently, the digital image correlation (DIC) technique has been utilized to study the Lüders band nucleation and propagation process during the tensile deformation of medium-Mn steels^[30–33]. Wang *et al.* found that the Lüders band nucleates at one grip end of a specimen and propagates through the entire parallel section to the other end at a constant velocity^[34]. The local Lüders strain is equivalent to the macroscopic Lüders strain and exhibits both space- and time-independent characteristics. Liu *et al.* found that Lüders strain and strain rate are intricately linked to factors such as yield stress, initial microstructure, and dislocation evolution^[35]. Among these, the Lüders-strain-rate emerges as a critical microstructure-sensitive factor highly associated with dislocation multiplication. This parameter can be characterized and quantified using advanced techniques such as scanning transmission electron microscopy (STEM) and synchrotron X-ray diffraction. A quantitative relationship between the Lüders-strain-rate and the dislocation multiplication rate has been established, providing insights into the Lüders banding phenomena observed in medium-Mn steels.

Besides the works on the dynamics of Lüders bands, research efforts are also increasingly focused on uncovering the microstructural and stress-state factors associated with Lüders banding, aiming to mitigate its impact and unlock the full industrial potential of these materials. For example, Varanasi *et al.* integrated

the electron channeling contrast imaging (ECCI) and macroscopic DIC to analyze the defect populations inside and across the Lüders front, identifying plastic zones, which align with the macroscopic Lüders front and exhibit a parallel arrangement, interspersed with the relatively lower deformation regions^[36]. However, current research has yet to fully elucidate the microstructural and stress states of the critical Lüders front. Further investigations are required.

This work employed the *in-situ* synchrotron HE-XRD technique to investigate the Lüders banding phenomenon in medium-Mn TRIP steel, focusing on the microstructural and stress states of the Lüders front. The results revealed an abnormal measured lattice strain asymmetry, based on which the local microstructural and stress states were discussed. The findings improve the understanding of the Lüders banding behavior in medium-Mn steels and demonstrate a rapid, effective method for studying the dynamics of similar localized deformation behaviors.

MATERIALS AND METHODS

Materials preparation

The experimental TRIP steel had a nominal composition (in mass%) of Fe-0.1C-10Mn-2Al, with the detailed measurement data provided in Table 1. Steel ingots were initially cast within a vacuum furnace to ensure high purity. Subsequently, the resulting 20-mm-thick plates underwent homogenization at 1,200 °C for 1 h to achieve a uniform microstructure, followed by hot rolling in the temperature range of 1,100–900 °C, reducing the thickness to 4 mm. Following hot rolling, the plates were cold rolled to a final thickness of 1.5 mm to achieve the desired deformation and refinement of the microstructure. The final samples for microstructure observation and mechanical tests were annealed at 650 °C for 1 h and then air-cooled to room temperature. Tensile tests were performed at room temperature using an Instron 3382 dual-column floor-mounted universal testing machine. The tests were conducted at a constant strain rate of 0.001 mm/s, with loading terminated upon reaching a total elongation of 5.5%. *In-situ* strain measurements were obtained from the tensile specimens using the DIC method.

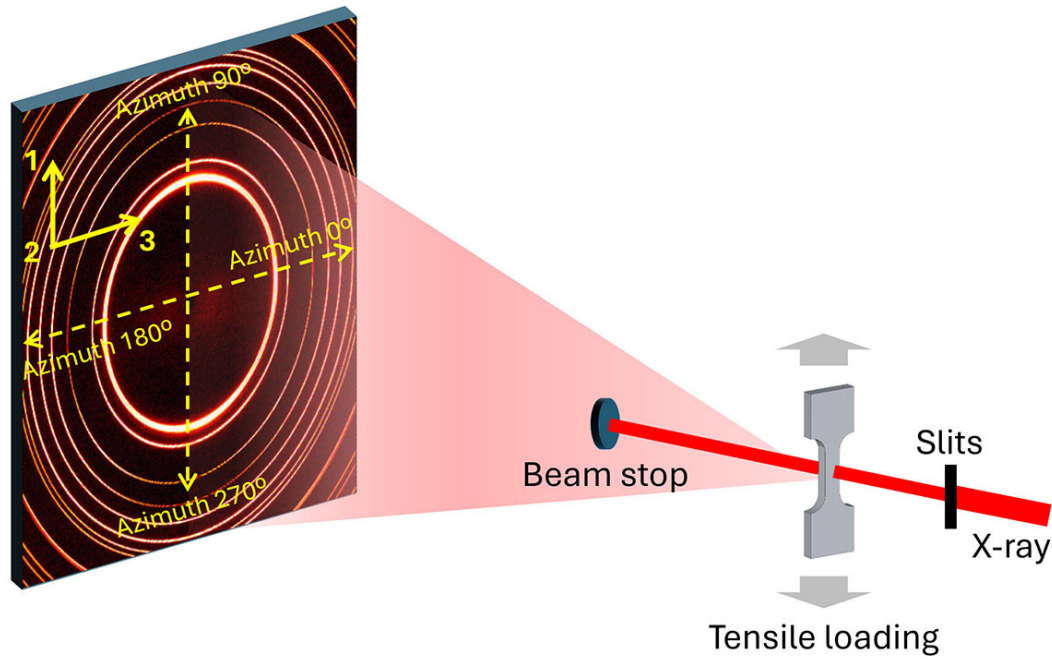
Microstructure characterization

The microstructure was characterized with a field emission scanning electron microscope (Zeiss Supra55) furnished with an Oxford electron backscatter diffraction (EBSD) detector using a step size of 35 nm. The specimen destined for EBSD characterization was initially ground successively with 150-grit to 3000-grit SiC papers, then polished using a diamond polishing compound with a particle size of 2.5 µm. Finally, it was subjected to electropolishing in a solution where the volume ratio of HClO₄ to C₂H₆O is 1:9 under a direct voltage of 20 V at room temperature. The scanning electron microscopy (SEM) specimens were etched in a 4% nitric acid solution after completing the aforementioned polishing procedures. Once the etching was complete, the specimens were immediately rinsed with ethanol to remove any residual etching solution from the surface.

The deformation behavior of the experimental steel was investigated by using the *in-situ* synchrotron-based HE-XRD technique at the 11-ID-C beamline of the Advanced Photon Source, Argonne National Laboratory (APS, ANL) in the US. The microstructure evolution and measured lattice strain changes of the specimen under uniaxial tensile loading were studied using a monochromatic X-ray beam with an energy of ~105 keV (wavelength 0.11742 Å). The setup of the *in-situ* HE-XRD loading experiment is illustrated in Figure 1. The beam size was set to be 300 µm × 300 µm. The dog-bone-shaped tensile specimen with dimensions of 0.5 mm in thickness, 10 mm in length, and 3 mm in width was mounted on a stress stage, with the rolling direction aligned parallel to the loading direction (LD). Two-dimensional (2D) diffraction patterns, consisting of smooth Debye rings, were collected at various loading levels during the tensile deformation at

Table 1. Chemical composition of the experimental Fe-0.1C-10Mn-2Al steel (mass%)^[37]

C	Mn	Al	Si	Fe
0.12	10.16	1.87	0.05	Bal

**Figure 1.** Schematic of *in-situ* HE-XRD loading experiment.

room temperature. Considering the propagative nature of the Lüders bands under increasing stress, a strain-controlled stepwise loading approach was adopted in this experiment to guarantee a constant diffraction volume during each exposure (10 s). This strategy aimed to maximize spatial resolution under the current experimental setup.

The experimental coordination system (axes 1-2-3) and azimuthal angle definition of the Debye rings are indicated in yellow in Figure 1. Cross-sectional data, where the scattering vector was parallel to various azimuths, were integrated to calculate the (azimuthal) measured lattice strain (to be explained later in the same paragraph) of various phases. The measured lattice strain, ε_{hkl} , was determined based on the relative change in the lattice plane spacing corresponding to the crystallographic plane (hkl), expressed as

$$\varepsilon_{hkl} = \frac{d_{hkl} - d_{0hkl}}{d_{0hkl}} \quad (1)$$

where d_{0hkl} and d_{hkl} denote the lattice spacings before and after applying stress at the test temperature, respectively. Note that the term “measured lattice strain” is used in this context to distinguish it from the commonly used “lattice strain”. In HE-XRD experiments, lattice strain calculations typically rely on certain assumptions, the most critical of which is that the irradiated volume is homogeneous regarding both microstructure and stress state. When this assumption is strictly met, the lattice strain calculated using Equation 1 corresponds to the true physical value, representing the elastic strain within the irradiated volume along the diffraction vector direction. However, due to the propagative nature of the Lüders bands,

this assumption may break down at certain critical loading steps in our case. As a result, the term “measured lattice strain” is used to account for potential inhomogeneities within the irradiated volume.

RESULTS AND DISCUSSION

Figure 2A displays the 2D XRD pattern of the initial medium-Mn TRIP steel, recorded over the full azimuthal angle range of 0° to 360° . The experimental steel exhibits an ultrafine-grained duplex microstructure comprising face-centered cubic (FCC) austenite (γ) and body-centered cubic (BCC) ferrite (α) phases. Crystallographic peaks of γ - $\{111\}$, γ - $\{200\}$, γ - $\{220\}$, γ - $\{311\}$, and α - $\{110\}$, α - $\{200\}$, α - $\{211\}$ are seen for the two phases. The non-uniform diffraction intensity distribution along the azimuthal angle indicates the presence of pronounced texture in the initial material. Microstructural analysis using EBSD [**Figure 2B** and **C**] reveals that the γ and α phases in the initial state exhibit similar morphologies, characterized by slightly elongated grains. The volume fractions of the two phases are 0.445 (γ) and 0.555 (α), respectively, which were calculated by classifying the EBSD data points.

Figure 3 illustrates the DIC strain field and SEM micrographs of three distinct microstructural regions. Samples used for the SEM characterizations were taken from a specimen deformed to a tensile strain of 0.055. This strain level corresponds to the point at which the Lüders band first interacted with the X-ray during the HE-XRD experiment (as detailed in the following sections). The microstructure of the undeformed region is displayed in **Figure 3A**, which consists of equiaxed α and γ grains, consistent with the EBSD results [**Figure 2B** and **C**]. The DIC strain field evolution depicted in **Figure 3B** captures the initial and intermediate yielding stages of the studied steel. During tensile testing, Lüders bands progressively propagate from the bottom to the top, with the macroscopic strain reaching 4.8% and the maximum local strain reaching $\sim 13\%$. The Lüders front keeps an angle of 85° to the macroscopic tensile loading direction. The microstructure at the Lüders front is shown in **Figure 3C**, revealing a multi-phase structure of α , γ , and lamellar martensite α' . The α' phase shares the same crystal structure and exhibits lattice parameters very similar to those of the α phase^[38]. Notably, the newly transformed lamellar martensite grains are oriented at approximately a 45° angle to the applied tensile direction, e.g., LD, highlighting the shear nature of the Lüders front deformation. **Figure 3D** presents the microstructure of the fully deformed region, which exhibits a higher volume fraction of martensite α' compared to the Lüders front. In this region, the lamellar martensite grains no longer maintain a 45° orientation to the applied tensile direction due to rigid rotation driven by the deformation of neighboring α and γ grains.

Figure 4 presents the engineering stress-strain curve obtained from the *in-situ* HE-XRD loading experiment of the investigated medium-Mn TRIP steel at room temperature. A general analysis of the phase transformation that occurred during the experiment can be found in^[37]. Here, we focus on the microstructural and stress states of the migrating Lüders front, with the Lüders plateau being boxed with dashed lines in red. The interested early deformation stage is magnified as an inset highlighting the selected strain points for analysis, distinguished by gradient colors. Among these, the strain point marked in purple, corresponding to a strain level of 0.055, represents the moment when the Lüders bands first interact with the X-ray beam. This critical strain point will be analyzed in detail in the following section.

The azimuth-dependent variation of integrated diffraction intensities for the two phases as Lüders banding progresses is illustrated in **Figure 5**. It is well-established that Lüders banding occurs through intense localized plastic deformation, often accompanied by significant texture changes and potentially coupled with strong phase transformation. The intensity distribution curves for five crystallographic planes, i.e., $\{200\}$, $\{220\}$, and $\{311\}$ of the FCC γ phase [**Figure 5A–C**] and $\{200\}$ and $\{211\}$ of the BCC α phase [**Figure 5D** and **E**], remain highly overlapped before the strain point of 0.055. This overlap indicates the

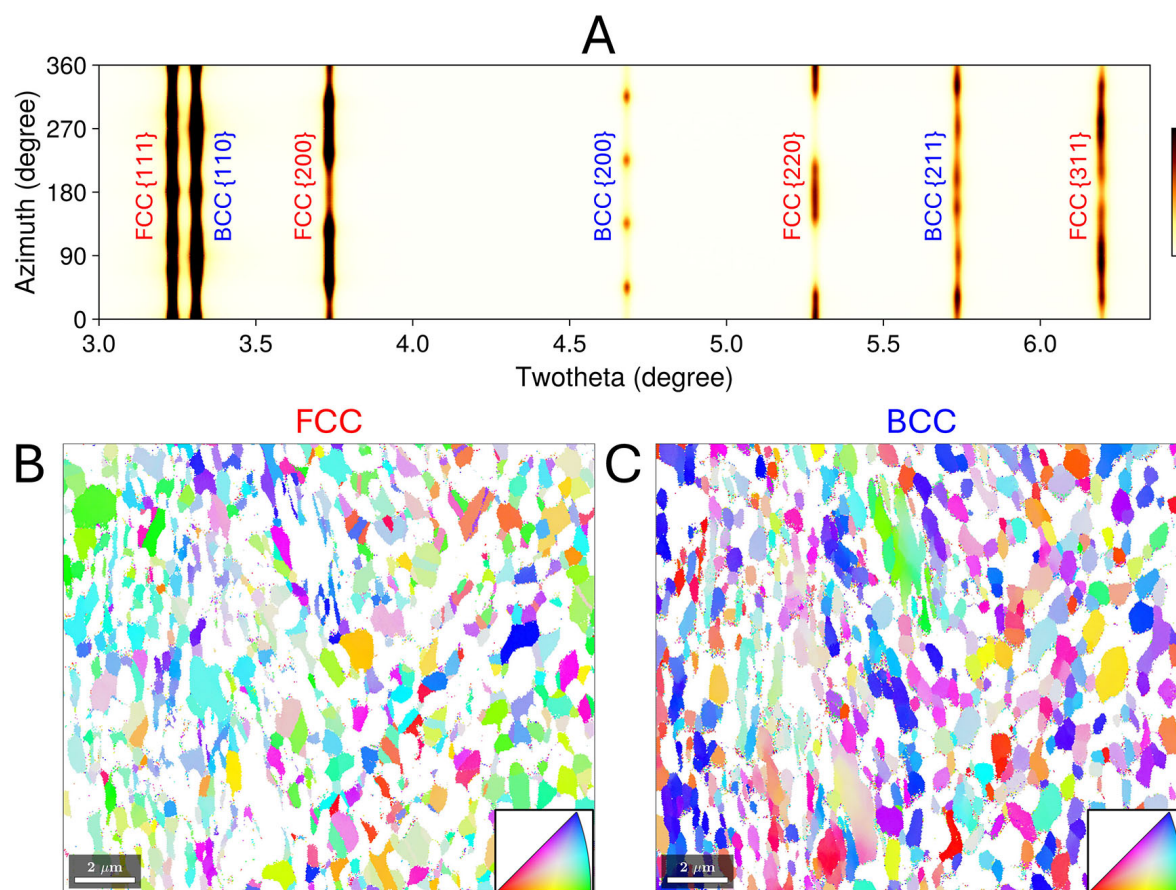


Figure 2. (A) 2D XRD pattern along the full azimuthal angle from 0° to 360° for the investigated medium-Mn TRIP steel of the initial state. Orientation images with inverse pole figure coloring along the azimuth 0° (axis-3 in Figure 1) for FCC γ phase (B) and BCC α phase (C). (For interpretation of the references to color in this figure legend, the reader is referred to the web version of this article).

absence of grain rotation, confirming that the irradiated volume remains in the elastic deformation stage. A slight change in the intensity distribution becomes identifiable when the strain point moves to 0.055, followed by a pronounced pattern change at the strain point of 0.06. Based on this, it can be reasonably inferred that the strain point of 0.055 (as highlighted in the legends of Figure 5) corresponds to the state where Lüders bands begin interacting with the X-ray beam. By the strain point of 0.06, the Lüders front has swept through the characterized volume. Furthermore, only a minimal phase transformation is observed at the strain point of 0.055, as evidenced by the modest change in the azimuthal intensity.

The variations in the peak full width at half maximum (FWHM) for the selected strain points are shown in Figure 6, based on which the degree of plastic deformation can be evaluated. Unlike in intensity, the FWHM curves for the critical 0.055 strain point exhibit a noticeable increase across all peaks compared to earlier strain points. However, this increase remains significantly lower than that observed at the 0.06 strain point, which corresponds to the state after complete Lüders banding. The peak broadening observed at 0.055 strain point indicates the onset of plastic deformation in the irradiated volume. At strain points of 0.06 and beyond, the broadening of FCC peaks is notably more pronounced than that of BCC peaks, indicating that Lüders banding predominantly involves the deformation of the γ phase. Back to the 0.055 strain point, as the peak broadening is relatively minor and we already know that the texture change is minimal from Figure 5, the Lüders banding volume is estimated to account for less than 25% of the irradiated volume at this strain

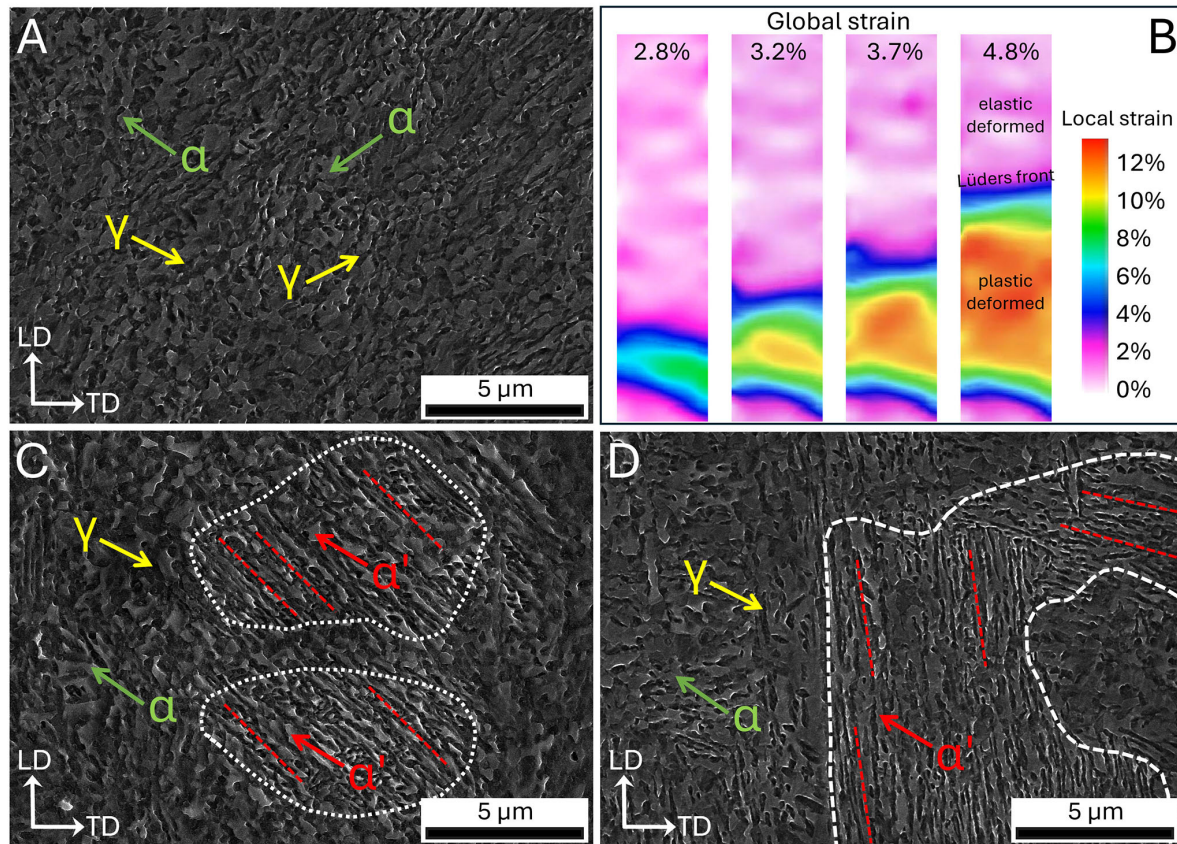


Figure 3. DIC strain field and SEM micrographs. (A) SEM micrograph of the undeformed region. (B) DIC strain field and localized strain. (C) SEM micrograph of the Lüders front region. (D) SEM micrograph of the plastically deformed region. LD and TD are aligned with the rolling and transverse directions of the sheet, respectively.

point. These findings further imply the presence of a plastic deformation gradient at the Lüders front, where phase transformation lags behind plastic deformation.

Based on the above analysis, the critical 0.055 strain point can be considered representative of the Lüders front. In this zone, plastic deformation initiates within a small portion of the irradiated volume without the occurrence of phase transformation. Next, we will analyze the stress state of the irradiated volume at this critical strain point.

Figures 7 and 8 illustrate the azimuth-dependent variations of measured lattice strains for crystallographic planes of the two phases at different applied strain levels (aligned to strain points of Figures 4–6). The curves prior to the critical strain point of 0.055 exhibit typical cosine-function-like shapes with the measured lattice strain values steadily increasing as deformation progresses [Figure 7A–C, Figure 8A and B]. After complete Lüders banding at the strain point of 0.06 and beyond, segments of these curves become much more distorted due to the intensifying grain-to-grain (and possibly phase-to-phase) plastic interaction. Despite these changes, clear symmetry lines can be identified at azimuthal angles of 0° (360°), 90° , 180° , and 270° for these curves. Specifically, the maximum measured lattice strain values obtained at azimuths of 90° and 270° are consistent, as are the minimum values obtained at 0° (360°) and 180° .

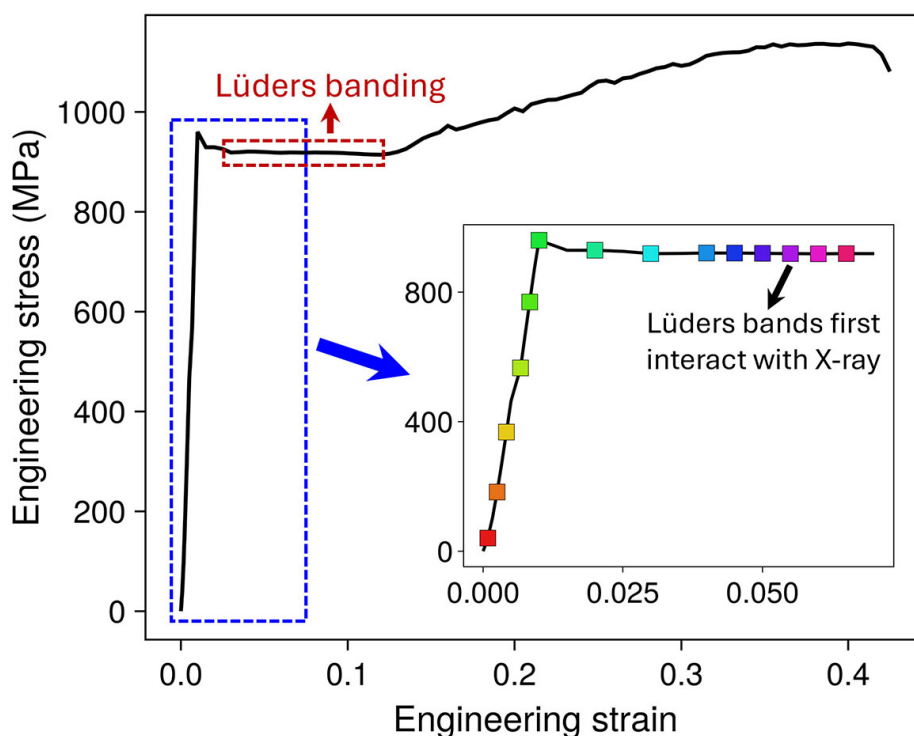


Figure 4. Engineering stress-strain curve of the medium-Mn TRIP steel during *in-situ* HE-XRD loading experiment^[37]. The inset magnifies the early deformation stage, highlighting the selected strain points. (For interpretation of the references to color in this figure legend, the reader is referred to the web version of this article).

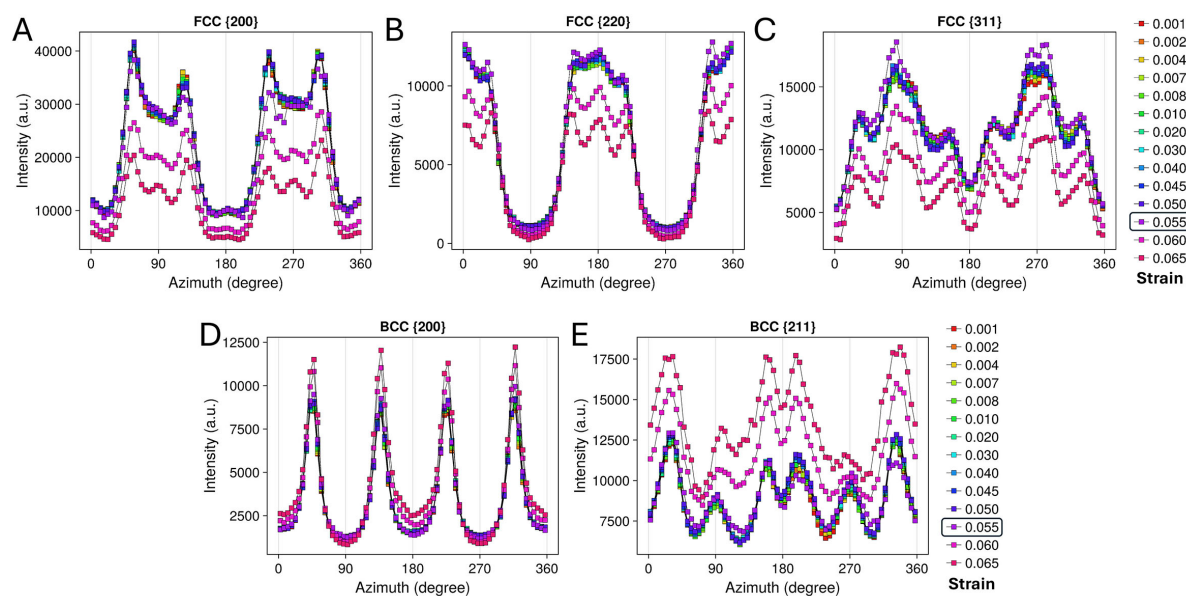


Figure 5. Integrated diffraction intensity as a function of azimuth for the FCC γ and BCC α' phases from a series of strain points. (A) FCC {200}. (B) FCC {220}. (C) FCC {311}. (D) BCC {200}. (E) BCC {211}. The strain-point color coding is consistent with that used in the inset of Figure 4. The boxed strain of 0.055 corresponds to the point at which the Lüders bands first interact with the X-ray. (For interpretation of the references to color in this figure legend, the reader is referred to the web version of this article).

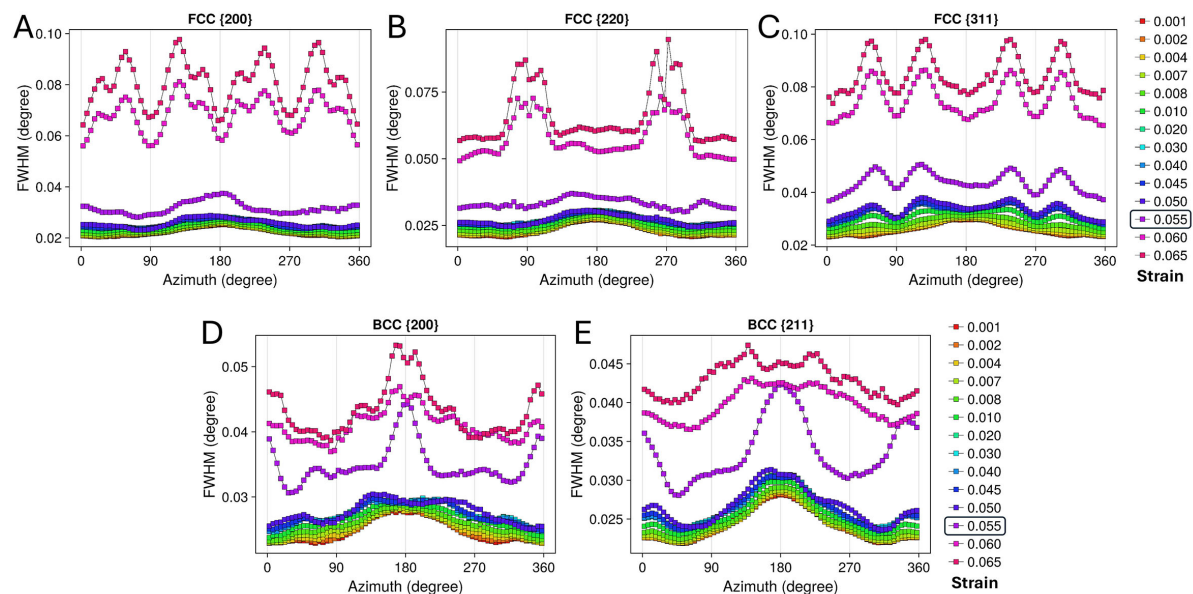


Figure 6. The peak full width at half maximum as a function of azimuth for the FCC γ and BCC α/α' phases from a series of strain points. (A) FCC {200}. (B) FCC {220}. (C) FCC {311}. (D) BCC {200}. (E) BCC {211}. The strain-point color coding is consistent with that used in the inset of Figure 4. The boxed strain of 0.055 corresponds to the point at which the Lüders bands first interact with the X-ray. (For interpretation of the references to color in this figure legend, the reader is referred to the web version of this article).

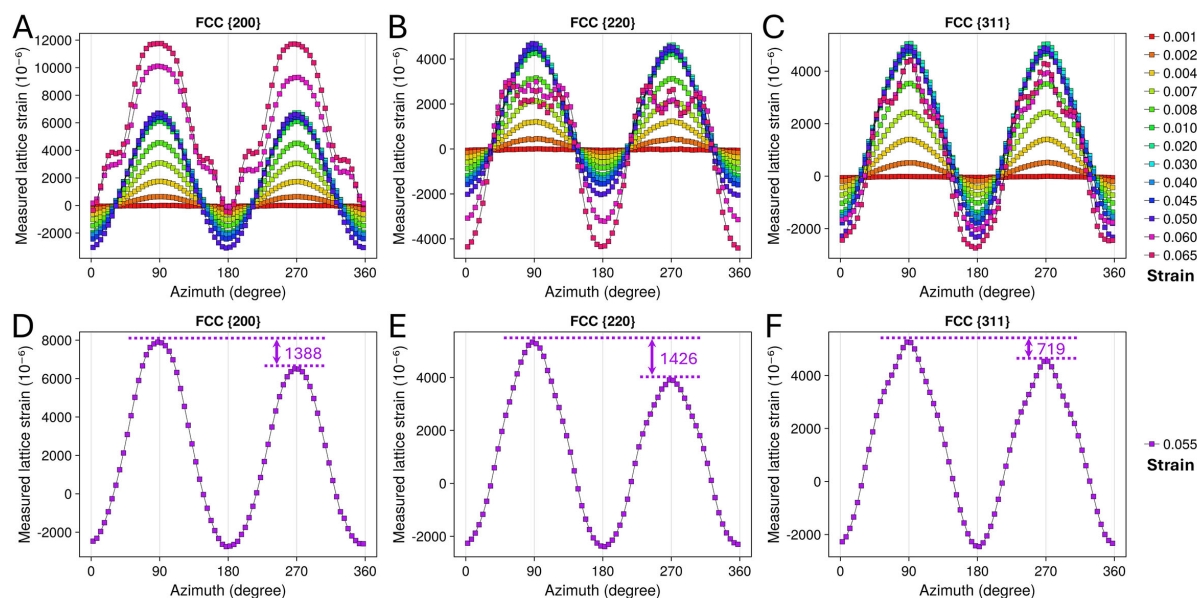


Figure 7. Measured lattice strain as a function of azimuth for the FCC γ phase. (A-C) Lattice strain data from a series of strain points beside 0.055. (D-F) Lattice strain data from the strain point of 0.055, where the Lüders bands first interact with X-rays. The strain-point color coding is consistent with that used in the inset of Figure 4. (For interpretation of the references to color in this figure legend, the reader is referred to the web version of this article).

The measured lattice strain distribution curves of the critical strain point of 0.055 for the γ and α/α' phases are respectively depicted in Figure 7D-F, Figure 8C and D. These curves closely resemble those at elastic strain points in the cosine-function-like shape [Figure 7A-C, Figure 8A and B], suggesting that most of the

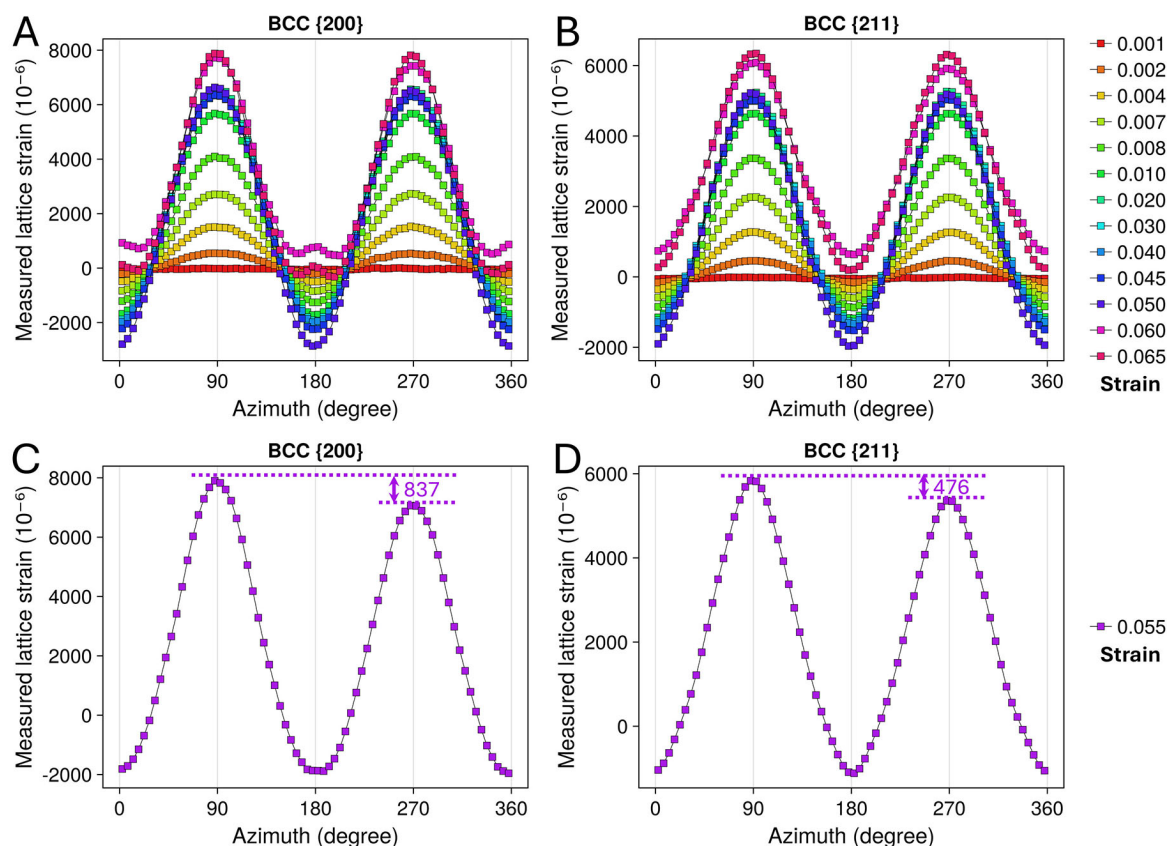


Figure 8. Measured lattice strain as a function of azimuth for the BCC α/α' phase. (A and B) Lattice strain data from a series of strain points beside 0.055. (C and D) Lattice strain data from the strain point of 0.055, where the Lüders bands first interact with X-rays. The strain-point color coding is consistent with that used in the inset of Figure 4. (For interpretation of the references to color in this figure legend, the reader is referred to the web version of this article).

irradiated volume at this strain point remains in the elastic stage. This observation aligns with the peak intensity and broadening analyses presented in Figures 5 and 6. A notable difference is observed across all analyzed peaks: the measured lattice strain values at azimuth 90° are consistently higher than those of azimuth 270°, as indicated in the figures and parametrically summarized in Table 2. Meanwhile, the minimum measured lattice strain values at azimuths 0° (360°) and 180° remain nearly identical. Such measured lattice strain asymmetry is likely to contain valuable information about the local stress state of the Lüders front, making it worthy of further discussion.

The factors contributing to the observed measured lattice strain asymmetry can be examined in terms of microstructure and stress within the irradiated volume. In most reported research employing the same HE-XRD technique, the irradiated volume is generally assumed to be homogeneous in terms of both microstructure and stress. Under stricter assumptions, such as homogeneous deformation upon uniaxial loads, the measured lattice strain would naturally equal the actual lattice strain, i.e., elastic strain. Now consider the present case: a small portion at the upper end of the irradiated volume undergoes severe plastic deformation. As a result, the diffraction peak from this plastically deformed part broadens significantly (may also shift along LD). This broadened and shifted peak, characterized by lower intensity, resembles a background signal when fitting the primary diffraction peak (which remains much more intense and sharper). The primary peak can be chiefly attributed to the elastically deformed portion of the irradiated

Table 2. Measured lattice strain data of the analyzed peaks

Crystallographic plane	FCC			BCC	
	{200}	{220}	{311}	{200}	{211}
Measured lattice strain / 10^{-6} (90°)	7,896	5,333	5,255	7,901	5,833
Measured lattice strain / 10^{-6} (270°)	6,508	3,907	4,536	7,064	5,357
Deviation/ 10^{-6}	1,388	1,426	719	837	476

volume. As schematically shown in [Figure 9](#), where the red lines represent the diffracted beam and Debye ring of the current state, while the dashed black lines indicate the previous state (pure elastic stage), the center of the elastically deformed part shifts downward compared to earlier strain points. Consequently, the recorded Debye ring on the detector moves synchronously toward the 270° azimuth direction, resulting in a lower 2θ angle (and higher measured lattice strain) at 90° azimuth. This condition can lead to the measured lattice strain asymmetry observed in the data.

In addition to the microstructural factor discussed above, special stress states can also lead to such measured lattice strain asymmetry. [Figure 10A](#) schematically shows the typical diffraction geometry under uniaxial loading, where the local principal stress axis aligns with the applied loading. Under this condition, the deviating angle (α_1) between the upper diffraction vector and the principal stress axis at 90° azimuth equals that at 270° azimuth (α_2). As a result, the normal stress components along the two diffraction vectors are consistent in magnitude, leading to a symmetric measured lattice strain distribution, as seen in the Debye rings at strain points besides 0.055 [[Figure 7A-C](#), [Figure 8A and B](#)]. Previous studies^[39,40] have examined the shear deformation characteristics of the Lüders front, suggesting that a shear stress state can exist in the Lüders front region, even under external uniaxial loading. As depicted in [Figure 10B](#), under the influence of the shear stress component at the Lüders front, the local principal stress axis is tilted by an angle of $\arctan(2\tau/\sigma)/2$, where σ represents the normal stress component along axis-1 (LD), and τ is the shear stress component on the 1-2 plane. As a result of this tilting, the angle (α_1' and α_2') between the diffraction vector and the new principal stress axis at 90° and 270° azimuths becomes significantly different (the difference between α_1' and α_2' is approximately 2θ under the condition of [Figure 10B](#)). This tilt causes the inconsistency between the normal stress components along the two diffraction vectors. Consequently, the measured lattice strains become asymmetric. This analysis aligns with the shear deformation characteristic as evidenced by the 45° angle of the lamellar martensite at the Lüders front [[Figure 3C and D](#)]. The emergence of the shear stress component may be associated with special microstructural features such as the arrangement of stacking faults or martensites.

Indeed, both factors discussed above can simultaneously trigger the measured lattice strain asymmetry. As such, it is challenging to isolate and deconvolute their effects based on the data collected in the current experimental setup. Another limitation for the HE-XRD experiment employed in this work is that, strictly speaking, it captures only the local dynamic response, i.e., the detailed evolution of microstructural and stress state at a fixed position of the tensile specimen, which is interacted by the Lüders front at a tensile strain of 5.5%. While this approach reveals key features of the Lüders band, it does not provide information about the migrating band front prior to or after this critical strain point. Future advances may be enabled by the use of high-energy X-rays with smaller beam sizes (e.g., a $5\ \mu\text{m} \times 5\ \mu\text{m}$ high-energy beam will soon be available at the ID07 beamline of the High Energy Photon Source, Beijing, China), in combination with more advanced loading setups, beam scanning strategies, and DIC. These developments will enable the capture of finer details of Lüders banding dynamics and provide deeper insights into the role of individual contributing factors.

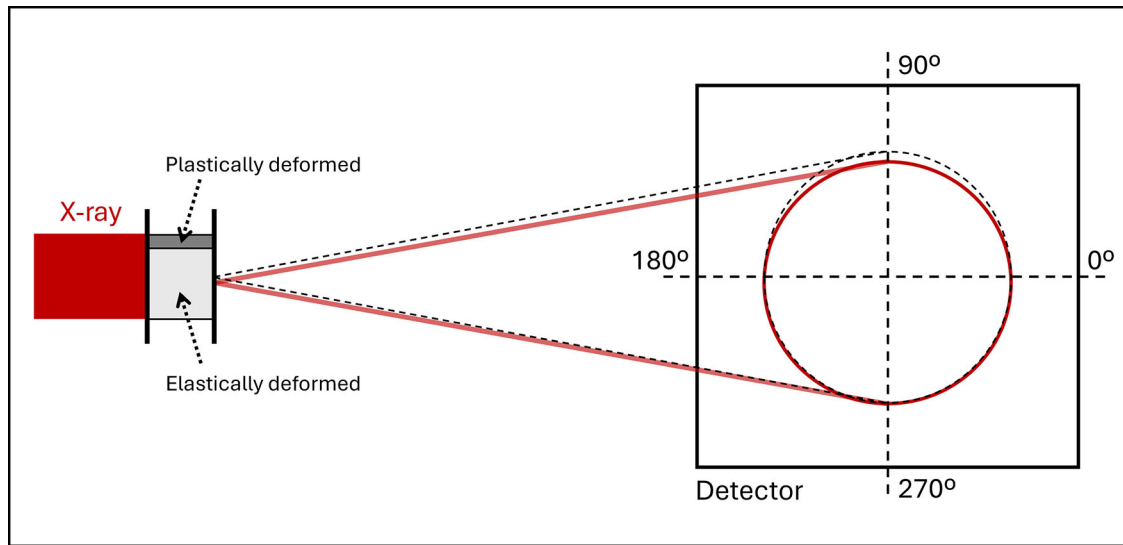


Figure 9. Schematic of the Debye ring shift on the detector due to the Lüders bands interacting with the X-ray.

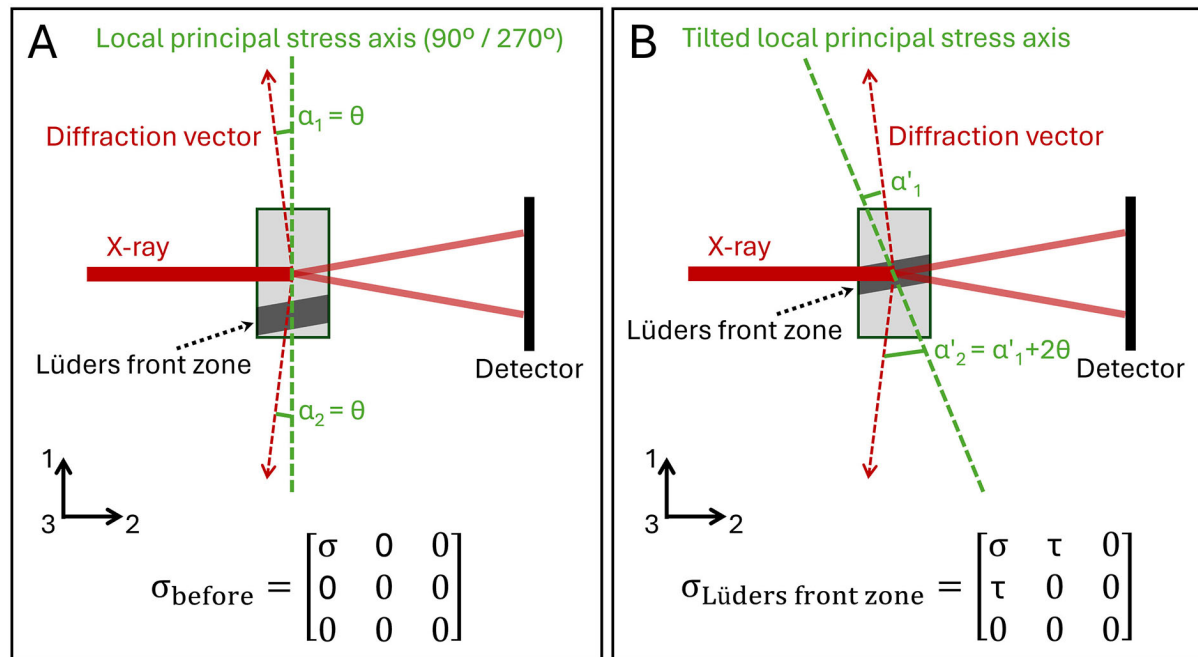


Figure 10. Schematic of the local stress state and the principal stress axis of the irradiated volume before (A) and when (B) overlapping with the Lüders front.

CONCLUSION

The high-energy X-ray diffraction patterns collected during an *in-situ* tensile loading test of a medium-Mn TRIP steel specimen were analyzed in terms of the intensity, full width at half maximum (FWHM), and measured lattice strain of diffraction peaks. The features of Lüders banding microstructure were examined based on the variations of azimuthal intensity and FWHM. An abnormal measured lattice strain asymmetry was noticed for all analyzed diffraction peaks at a critical strain point, where the Lüders front begins to enter the irradiated volume. The potential microstructural and stress factors that may trigger such asymmetry

were discussed, with the possibility of a local shear stress component and tilted principal stress axes at the Lüders front being proposed. Further insights into the Lüders band dynamics are expected to be obtained by refining the synchrotron high-energy X-ray diffraction technique and optimizing experimental strategies.

DECLARATIONS

Authors' contributions

Design: Zhang, M.; Li, R.

Experiments: Zhang, M.; Jia, J.; Jia, Z.

Manuscript writing: Zhang, M.; Jia, J.; Li, R.

Manuscript revision and supervision: Feng, Y.; Ma, Z.; Wang, Y. D.; Li, R.

Availability of data and materials

The raw data supporting the conclusions of this article are available from the corresponding author upon reasonable request.

Financial support and sponsorship

This work was financially supported by the National Natural Science Foundation of China (NSFC) (Grant Nos. 51901078), the Natural Science Foundation of Hebei Province (Grant No. E2022209070), Central Government Guided Local Science and Technology Development Funding Project (Grant No. 236Z1003G), and the Tangshan City Science and Technology Plan Project (Grant No. 24130207C). The use of the Advanced Photon Source is supported by the U. S. Department of Energy, Office of Science, Office of Basic Energy Sciences, under Contract No. DE-AC02-06CH11357. Li R and Ma Z are grateful to Prof. Matthew R Barnett for providing research fellow positions financially supported by Laureate Fellowship FL210100147.

Conflicts of interest

Wang, Y. D. is a member of the Senior Editorial Board for the journal *Microstructures*. Wang, Y. D. was not involved in any steps of editorial processing, notably including reviewer selection, manuscript handling, or decision making, while the other authors have declared that they have no conflicts of interest.

Ethical approval and consent to participate

Not applicable.

Consent for publication

Not applicable.

Copyright

© The Author(s) 2025.

REFERENCES

1. Suh, D. W.; Kim, S. J. Medium Mn transformation-induced plasticity steels: recent progress and challenges. *Scr. Mater.* **2017**, *126*, 63-7. [DOI](#)
2. Aydin, H.; Essadiqi, E.; Jung, I. H.; Yue, S. Development of 3rd generation AHSS with medium Mn content alloying compositions. *Mater. Sci. Eng. A.* **2013**, *564*, 501-8. [DOI](#)
3. Guo, Z.; Li, L.; Yang, W.; Sun, Z. Microstructures and Mechanical properties of high-Mn TRIP steel based on warm deformation of martensite. *Metall. Mater. Trans. A.* **2015**, *46*, 1704-14. [DOI](#)
4. He, B. B.; Huang, M. X. Strong and ductile medium Mn steel without transformation-induced plasticity effect. *Mater. Res. Lett.* **2018**, *6*, 365-71. [DOI](#)
5. Han, J.; Lee, S. J.; Jung, J. G.; Lee, Y. K. The effects of the initial martensite microstructure on the microstructure and tensile properties of intercritically annealed Fe-9Mn-0.05C steel. *Acta. Mater.* **2014**, *78*, 369-77. [DOI](#)
6. Hu, J.; Li, X.; Meng, Q.; Wang, L.; Li, Y.; Xu, W. Tailoring retained austenite and mechanical property improvement in Al-Si-V

- containing medium Mn steel via direct intercritical rolling. *Mater. Sci. Eng. A*. **2022**, *855*, 143904. DOI
7. Tian, G.; Xiao, J.; Bao, Z.; Yao, S.; Yan, L.; Zhao, A. Achieving 1.5 GPa grade medium Mn steel with high ductility via interrupted intercritical annealing process. *Mater. Sci. Eng. A*. **2024**, *905*, 145943. DOI
8. Bai, S.; Xiao, W.; Niu, W.; Li, D.; Liang, W. Microstructure and mechanical properties of a medium-Mn steel with 1.3 GPa-strength and 40%-ductility. *Materials* **2021**, *14*, 2233. DOI PubMed PMC
9. Chen, P.; Wang, J.; Li, X. W. Investigation of the hot-rolled medium-Mn steels with ultra-high strength and considerable ductility. *J. Mater. Eng. Perform.* **2025**, 1-6. DOI
10. Lan, H.; Lin, G.; Ma, Y.; Hu, B.; Du, L. Influence of intercritical annealing on microstructure, ductility, and toughness of medium Mn steels. *J. Mater. Eng. Perform.* **2025**, *34*, 14272-84. DOI
11. Steineder, K.; Krizan, D.; Schneider, R.; Béal, C.; Sommitsch, C. On the microstructural characteristics influencing the yielding behavior of ultra-fine grained medium-Mn steels. *Acta. Mater.* **2017**, *139*, 39-50. DOI
12. Heo, Y. U.; Suh, D. W.; Lee, H. C. Fabrication of an ultrafine-grained structure by a compositional pinning technique. *Acta. Mater.* **2014**, *77*, 236-47. DOI
13. Wang, S.; Chen, W.; Zhao, Z.; Zhao, X.; Luo, X.; Wang, Q. Effect of microstructure evolution on Lüders strain and tensile properties in an intercritical annealing medium-Mn steel. *J. Iron. Steel. Res. Int.* **2021**, *28*, 762-72. DOI
14. Ma, J.; Lu, Q.; Sun, L.; Shen, Y. Two-step intercritical annealing to eliminate Lüders band in a strong and ductile medium Mn steel. *Metall. Mater. Trans. A*. **2018**, *49*, 4404-8. DOI
15. Emadoddin, E.; Akbarzadeh, A.; Daneshi, G. Correlation between Luder strain and retained austenite in TRIP-assisted cold rolled steel sheets. *Mater. Sci. Eng. A*. **2007**, *447*, 174-9. DOI
16. Mao, W.; Gao, S.; Gong, W.; Harjo, S.; Kawasaki, T.; Tsuji, N. Quantitatively evaluating the huge Lüders band deformation in an ultrafine grain stainless steel by combining in situ neutron diffraction and digital image correlation analysis. *Scr. Mater.* **2023**, *235*, 115642. DOI
17. Wang, X.; Liu, C.; He, B.; Jiang, C.; Huang, M. Microscopic strain partitioning in Lüders band of an ultrafine-grained medium Mn steel. *Mater. Sci. Eng. A*. **2019**, *761*, 138050. DOI
18. Wang, X.; He, B.; Liu, C.; Jiang, C.; Huang, M. Extraordinary Lüders-strain-rate in medium Mn steels. *Materialia* **2019**, *6*, 100288. DOI
19. Benzing, J. T.; Luecke, W. E.; Mates, S. P.; Ponge, D.; Raabe, D.; Wittig, J. E. Intercritical annealing to achieve a positive strain-rate sensitivity of mechanical properties and suppression of macroscopic plastic instabilities in multi-phase medium-Mn steels. *Mater. Sci. Eng. A. Struct. Mater.* **2021**, *803*, 140469. DOI PubMed PMC
20. Liu, R.; Hu, Z.; Lin, C.; et al. A novel design to eliminate Lüders band in medium-Mn steel and its microstructure-property relationship. *Crystals* **2023**, *13*, 936. DOI
21. Qiu, H.; Ueji, R.; Inoue, T. Yield-point phenomenon and plastic bands in ferrite-pearlite steels. *Materials* **2022**, *16*, 195. DOI PubMed PMC
22. Mao, W.; Gao, S.; Gong, W.; et al. Martensitic transformation-governed Lüders deformation enables large ductility and late-stage strain hardening in ultrafine-grained austenitic stainless steel at low temperatures. *Acta. Mater.* **2024**, *278*, 120233. DOI
23. Fu, J.; Liu, W.; Sui, H.; Cheng, Y.; Duan, H. Simulations of the localized necking and Lüders band in irradiated metals by crystal plasticity. *Acta. Mech. Sin.* **2023**, *39*, 22339. DOI
24. Sarafanov, G. F.; Shondin, Y. G. Deformation instability in crystalline alloys: Lüders bands. *Mater. Phys. Mech.* **2021**, *47*. DOI
25. Sun, B.; Ma, Y.; Vanderesse, N.; et al. Macroscopic to nanoscopic in situ investigation on yielding mechanisms in ultrafine grained medium Mn steels: Role of the austenite-ferrite interface. *Acta. Mater.* **2019**, *178*, 10-25. DOI
26. Ma, Y.; Sun, B.; Schökel, A.; et al. Phase boundary segregation-induced strengthening and discontinuous yielding in ultrafine-grained duplex medium-Mn steels. *Acta. Mater.* **2020**, *200*, 389-403. DOI
27. Liang, Z.; Cao, Z.; Lu, J.; Huang, M.; Tasan, C. Influence of co-existing medium Mn and dual phase steel microstructures on ductility and Lüders band formation. *Acta. Mater.* **2021**, *221*, 117418. DOI
28. Luo, H.; Dong, H.; Huang, M. Effect of intercritical annealing on the Lüders strains of medium Mn transformation-induced plasticity steels. *Mater. Des.* **2015**, *83*, 42-8. DOI
29. Zhang, M.; Li, R.; Ding, J.; et al. In situ high-energy X-ray diffraction mapping of Lüders band propagation in medium-Mn transformation-induced plasticity steels. *Mater. Res. Lett.* **2018**, *6*, 662-7. DOI
30. Yan, S.; Yu, Z.; Liang, T.; et al. Unusual step-like stress flow behavior and mechanisms of a 1.3 GPa grade medium-Mn steel with 51.2% ductility. *Mater. Des.* **2023**, *235*, 112380. DOI
31. Han, J.; Wang, J.; Manladan, S. M.; et al. Effect of Lüders bands by strain ageing on strain distribution, microstructure and texture evolution of high-strength pipe steel. *Acta. Metall. Sin.* **2021**, *34*, 657-67. DOI
32. Ma, J.; Liu, H.; Lu, Q.; Zhong, Y.; Wang, L.; Shen, Y. Temperature-dependent macroscopic mechanical behaviors and their microscopic explanations in a medium Mn steel. *Metall. Mater. Trans. A*. **2020**, *51*, 5180-6. DOI
33. Liu, Y.; Jiang, J.; Li, Y.; et al. Correlation of TRIP effect and Lüders band in a 2.3 GPa ultra-high yield strength medium Mn steel with martensite matrix. *Mater. Sci. Eng. A*. **2025**, *930*, 148172. DOI
34. Wang, X.; Wang, L.; Huang, M. Kinematic and thermal characteristics of Lüders and Portevin-Le Châtelier bands in a medium Mn transformation-induced plasticity steel. *Acta. Mater.* **2017**, *124*, 17-29. DOI
35. Liu, C.; Hu, C.; Wang, X.; Huang, M.; Jiang, C. A new perspective on Lüders band formation in medium-Mn steels based on Lüders-

- strain-rate and dislocation evolution. *Mater. Sci. Eng. A*. **2024**, *901*, 146553. DOI
36. Varanasi, R. S.; Zaefferer, S.; Sun, B.; Ponge, D. Localized deformation inside the Lüders front of a medium manganese steel. *Mater. Sci. Eng. A*. **2021**, *824*, 141816. DOI
 37. Zhang, M.; Tan, Q.; Ding, J.; et al. In situ high-energy X-ray diffraction investigation of the micromechanical behavior of Fe-0.1C-10Mn-0/2Al steel at room and elevated temperatures. *Mater. Sci. Eng. A*. **2018**, *729*, 444-51. DOI
 38. Lobodyuk, V. A.; Meshkov, Y. Y.; Pereloma, E. V. On tetragonality of the martensite crystal lattice in steels. *Metall. Mater. Trans. A*. **2019**, *50*, 97-103. DOI
 39. Maruyama, N.; Yamamoto, M.; Tabata, S. Microscopic shear deformation characteristics of the Lüders front in a metastable austenitic transformation-induced-plasticity steel. *ISIJ. Int.* **2023**, *63*, 899-909. DOI
 40. Shariat, B. S.; Li, Y.; Yang, H.; Wang, Y.; Liu, Y. Shear strain evolution during tension-induced Lüders-type deformation of polycrystalline NiTi plates. *Mater. Sci. Eng. A*. **2022**, *839*, 142774. DOI